

Elucidating the hydrogen adsorption kinetics on Pt/TiO₂/Pt based highly efficient sensors

Azhar Ali Haidry^{1,2,3*}, Yinwen Ji^{1,2}, Adil Raza¹, Hao Zhu^{1,2}, Ali Zavabeti⁴, Bilge Saruhan⁵

¹College of Materials Science and Technology, Nanjing University of Aeronautics and Astronautics, 211100 Nanjing, China

²Key Laboratory of Materials Preparation and Protection for Harsh Environment, Ministry of Industry and Information Technology, 211100 Nanjing, China

³Department of Physics, University of Okara, 2 KM Multan Road Renala Khurd By Pass, Okara-Pakistan

⁴Department of Chemical Engineering, the University of Melbourne, Victoria, Parkville 3010, Australia

⁵German Aerospace Center (DLR), Institute of materials research, Linder Hoehe, 51147 Cologne, Germany

*Corresponding author: aa.haidry@nuaa.edu.cn, Tel.: 0086-18851870739

Nomenclature

A	Geometric electrode surface area (cm ²)
α	The rate constant of sorption defined in Eq. (S8) (g/mg min)
a	Initial adsorption rate defined in Eq. (S1) (mg/ (g min))
b	Elovich constant defined in Eq. (S1) (g/mg)
C _{H₂}	Concentration of H ₂
C _i	Constant defined in Eq. (S4) (mg/g)
IPD	Inter-particle diffusion model
IDEs	Inter-digitated electrodes
K	The rate constant of sorption defined in Eq. (S9) (g/mg min)
k	The pseudo-second-order rate constant defined in Eq. (5) (g mg ⁻¹ min ⁻¹)
k _a	The rate constant of sorption defined in Eq. (S6) (g/mg min)
k _{id}	ID rate constant defined in Eq. (4) (mg/g min ^{1/2})
k ₂	Lagergren's first-order rate constant defined in Eq. (1) (min ⁻¹)
k ₃	The rate constant of sorption defined in Eq. (7) (g/mg min)
kq _e ²	The initial adsorption rate defined in Eq. (7) (mg g ⁻¹ min ⁻¹)
L	Length of the top electrode of the sensor (mm)
N	Avogadro's constant (mol ⁻¹)
n	Order of the reaction defined in Eq. (S6)

n_0	Amount of adsorption at equilibrium defined in Eq. (3) (mg/g)
n_{ads}	Rate of adsorbed species defined in Eq. (S5) (counts s ⁻¹)
n_s	Counting rate of the solution background defined in Eq. (S5) (counts s ⁻¹)
ppm	Parts per million
PFO	Pseudo-first-order
PSO	Pseudo-second-order
q	Amount of adsorption at time $t = t$ defined in Eq. (S8) (mg/g)
q_e	Amount of adsorption at equilibrium defined in Eq. (5) (mg/g)
q_t	Amount of adsorption at time $t = t$ defined in Eq. (5) (mg/g)
q_∞	Amount of adsorption at equilibrium defined in Eq. (S8) (mg/g)
R	Resistance (Ω)
R^2	Coefficient of correlation
R_{air}	Resistance of the sensor in technical air (Ω)
R_{gas}	Resistance of the sensor in specified gas (Ω)
R_{H_2}	Resistance of the sensor in technical air with H ₂ (Ω)
RT	Room temperature ($^{\circ}\text{C}$)
S	Real electrode surface area (cm ²)
SC-PSO	Sobkowski and Czerwinski pseudo-second order
S_R	Sensor response
S_{RH_2}	The sensor response to H ₂
S_{RX}	The sensor response to other specified gases
Scm	Standard cubic centimeter per minute (ml/min)
T	The thickness of the TiO ₂ layer (mm)
$T_i^{\bullet\bullet\bullet\bullet}$	Titanium interstitial
T_{rec}	Recovery time (seconds)
T_{res}	Response time (seconds)
t	Adsorption time (min)
μ	Adsorption coefficient defined in Eq. (S5)
$V_o^{\bullet\bullet}$	Double electron ionization of oxygen vacancy
W_R	Weight fraction (%)
θ_e	Amount of adsorption at equilibrium (mg/g)
θ_t	Amount of adsorption at time $t = t$ (mg/g)
Γ	The surface (Pt) concentration at time $t=t$ defined in Eq. (S5) (molecules/cm ²)
Γ_e	The surface (Pt) concentration after the completion of the reaction (molecules/cm ²)

Abstract

The adsorption of a gas and its concomitant diffusion onto the semiconductor surface are the primary factors to determine the response of a gas sensor. Despite intensive sensor research, understanding the gas adsorption reaction kinetics has been protractedly ignored. The current study is riveted on elucidating the adsorption kinetics of hydrogen gas onto the Pt/TiO₂/Pt structured sensors. It is demonstrated that the prepared Pt/TiO₂/Pt structure features excellent hydrogen sensing performances (sensor response $\sim 10^4$ at room temperature) increased to $\sim 10^6$ at 100 °C toward 10,000 ppm H₂. More importantly, the adsorption kinetics are investigated by verifying the experimental results against various theoretical models. It is found that Ho's pseudo-second-order model (H-PSO) fits well with the experimental results having correlation factors higher than 0.99 for almost all gas concentrations and operating temperatures. Eventually, the H₂ adsorption kinetics onto Pt/TiO₂/Pt structure are meticulously analyzed based on the correlation between experimental results and theory.

Keywords: Adsorption; Hydrogen sensing; Reaction kinetics; TiO₂; Second-order rate equation

1. Introduction

Owing to its renewable and environment-friendly nature, hydrogen (H₂) gas is inevitably a promising candidate for clean energy. Moreover, hydrogen is intensively used in the production of various volatile compounds (such as ammonia production and methyl alcohol) in the petrochemical industry, the manufacturing of glass/steel, and rocket propulsion systems [1-4]. Due to its odorless, colorless, and explosiveness nature, specifically when its certain concentration (4-75 volume percent) is mixed with air, the detection of hydrogen has become majorly critical during the handling processes, storage production, and transportation [2, 5]. In this context, TiO₂ has proved to be the most promising, being highly stable under harsh conditions [1-7]. In addition, the sandwiched type structure Pt/TiO₂/Pt has shown excellent sensitivity even at room temperature, long-term stability, and low manufacturing cost [8-19].

Despite the improved sensing characteristics of gas sensors based on metal oxides, there is minuscule work that focuses on the gas adsorption kinetics, hence, imparting an unclear explanation of the origin of such high sensitivities. Furthermore, the destitute knowledge of the reaction kinetics of gases onto the surface of materials that have not been studied to their potential leads to divergent interpretations of the sensing mechanism. Therefore, this ongoing study attempted to elucidate the H₂ adsorption kinetics on the Pt/TiO₂/Pt surface. The present study, besides the existing knowledge of the H₂ sensing mechanism, adds in-depth fundamental insights proving highly important for the development of future gas sensing devices.

2. Material and methods

All the chemicals and reagents in this work were high purity analytically (AR) graded and used with no further purification, unless otherwise mentioned.

2.1 Sensor fabrication

Polycrystalline alumina (corundum) substrates were purchased from Siegert Thin Film Technology GmbH (Germany). A series of sensors based on Pt/TiO₂/Pt structure were prepared on mechanically polished and chemically cleaned corundum (Al₂O₃) substrates with dimensions L×W×T=20×10×0.65 mm by the standard metallographic procedure. The archetypal schematic of the sensor fabrication process is shown in **Fig. 1** and the typical procedure is described as follows. An in-house laser patterned Ferrum mask (with dimensions L×W×T=18×8×0.05 mm) was used to fabricate both the bottom and top Pt electrodes (labeled as BE and TE, respectively). First, the deposition of Pt-BE stripes (L×W×T= 12×1× (2×10⁻⁴) mm) was done by sputter deposition of Pt target (99.99% purity) in BAL-TEC SCD 500 Sputter Coater (BAL-TEC GmbH, Germany). The sputtering process was performed for 2 minutes with an overall chamber pressure of less than 0.01 mbar, which resulted in an approximately ~200 nm thin Pt coating. Then, in the second step, the 2 μm thick TiO₂ coatings were prepared by radio frequency (r. f.) reactive magnetron sputtering equipment Z400 from the SVS–Vacuum coating Technologies–Systec Group (Germany). For this purpose, high-purity Ti targets (99.95%) were employed for the deposition of TiO₂ in the plasma sputtering chamber under a mixture of Ar+O₂ atmosphere. In this process, a sputtering power of 800 Watts was applied on Ti-target under Ar+O₂ flow (27.4 and 5.7 sccm respectively) for 8 hours, yielding ~2 μm thick TiO₂ coating. During the deposition process, no substrate heating was

applied. In the third step, the top Pt electrode cross-bar stipes (Pt-TE) with the same procedure and dimension as Pt-BE were deposited. This culminates in the fabrication of Pt/TiO₂/Pt sensing structures, which were annealed in static compressed air at 800 °C for 3 hours with a heating rate of 100 °C/15 min in the muffle furnace (KR 170E) from Heraeus Instruments GmbH (Germany). Similarly, a series of five sensor samples was prepared.

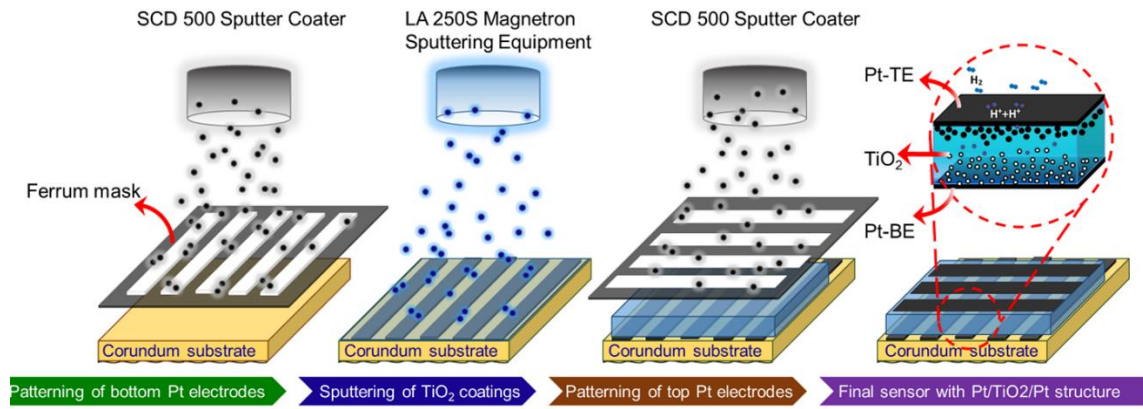


Figure 1. The schematic illustration of Pt/TiO₂/Pt sensor fabrication process.

2.2 Characterization

The prepared Pt/TiO₂/Pt structures were characterized for structural, morphological, and chemical composition by X-ray diffraction (XRD, SIEMENS D5000, Germany) with a CuK α radiation ($\lambda_{\text{CuK}\alpha} = 0.15418$ nm), scan rate of 10°/min, scan step of 0.02° and the graphite curved monochromator, field emission scanning electron microscope (FE-SEM, Ultra 55 from Zeiss, Germany), energy dispersive X-ray spectrometer (EDX) having an X-Ray Fluorescence Analyzer MESA 500 (Oxford Instruments), and glow discharge optical emission spectrometer (GDOES GDA 650, Spectrum Analytic GmbH, Germany) equipped with charge-coupled device (CCD) detector. For further details of the characterization procedure, the reader is referred to our previously published paper [15, 20].

2.3 Sensor tests

In this work, the gas sensors based on Pt/TiO₂/Pt structured sensors were executed with an indigenously established in-house built-in computer-controlled gas sensor test unit (SESAM) at the Institute of Materials Research of the German Aerospace Center (DLR)–Cologne. Here

throughout the manuscript, the room temperature is referred to as RT~20 °C, which was the average temperature maintained in our lab SESAM during the complete sensor tests. The relative humidity (%RH) in our SESAM lab is typically 30% RH this is because the test unit is placed inside a room with a controlled environment to avoid any environmental impact. The sensors are placed inside a quartz-glass tube (stable up to 1300 °C) having a 3 m tube for heating of gas mixture, which is then placed in a computer-controlled tubular furnace (CARBOLITE) allowing the heating up to 1200 °C. This arrangement allows tests of flexible sample geometry (max. \varnothing ~50 mm). The room temperature measurements were performed with no heating, while heat is supplied by a tubular furnace for gas sensor tests at higher temperatures (50 °C and 100 °C). The sensors were kept at this temperature for at least 1 h before tests so that the sensor resistance becomes stable. In SESAM, all the included instruments were remotely controlled by custom-made LabVIEW software. The gas sensing test unit is equipped with in-house data acquisition LabVIEW software, the gas mixing chamber, and a highly stable (under extreme temperatures and pressure) response test chamber with a volume of 200 cm³. Several mass flow controllers from MKS Instruments GmbH (MFC-647b) were used to precisely control eight gas flow channels simultaneously under a fixed gas flow regime of 400 mL/min. Keithley 2635A Source meter (Keithley, Tektronix DE) DC-measurement was used to supply a constant current of 1.0 μ A (1.0 V) to measure the dynamic electrical resistance (or conductance). To ensure good electrical contact between the Pt electrodes of the sample and low noise triaxial cable (Model 237-TRX-NG) of the Keithley source meter, thin Pt wires (wires \varnothing ~0.1 mm) and highly conductive silver paste solder were used. The setup allows measuring very high resistance (up to ~100 G Ω) with low noise and the changes in resistance, current, or voltage of the sample. The test gas (H₂) concentrations were varied in the range of 150–10000 ppm in dry technical air background, see **Fig. S1** in the supplementary data.

3. Results and discussion

3.1 Basic characterization

Notably, in comparison to the samples annealed at 800°C the as-deposited samples mostly showed an amorphous phase and then resulted in poor H₂ sensing properties, hence the annealed samples are the main focus in this study in terms of results and discussion. The comparative X-ray

diffractograms of as-deposited and annealed (800°C) Pt/TiO₂/Pt samples are shown in **Fig. 2**. It can be observed that the characteristic peak positions of annealed samples are well compatible with the standard diffraction data JCDS 21-1272 of tetragonal anatase of space group I4₁/amd with $a=b = 3.78 \text{ \AA}$ and $c = 9.522 \text{ \AA}$, JCDS 21-1276 of tetragonal rutile of space group P4₂/mnm with $a = b = 4.5933 \text{ \AA}$, $c = 2.9592 \text{ \AA}$ and JCDS 04-0802 of the cubic platinum crystal structure of space group $Fm\bar{3}m$ with $a = 3.9231 \text{ \AA}$. The corresponding results exhibit characteristic peaks from the bulk powder diffracted anatase A(101) at $2\theta \sim 25.3^\circ$ and rutile R(110) at $2\theta \sim 27.4^\circ$ phases, which are greatly in agreement with the previous findings. Furthermore, the diffractograms of annealed samples show major reflection planes of R(101), Pt(111), R(111), Pt(200), A(200), and R(211) at $2\theta \sim 36.11^\circ$, $2\theta \sim 39.8^\circ$, $2\theta \sim 41.2^\circ$, $2\theta \sim 46.4^\circ$, $2\theta \sim 48.0^\circ$ and $2\theta \sim 54.3^\circ$. Markedly, an unanticipated A(004) peak slightly shifted to a higher degree at $2\theta \sim 37.88^\circ$ corresponding to the anatase phase was seen to be even stronger than the powder diffraction peak of A(101) and R(110). This demonstrates that the anatase phase at A(004) plane is preferentially orientated along with the Pt(111) plane and grew to exhibit an extended c-axis orientation owing to epitaxial force between TiO₂ and Pt, thus intriguing a quasi-epitaxial growth of TiO₂ at Pt(111) surface [21]. To further the XRD analysis, the grain size for the strong anatase phase A(004) of the samples was estimated using the Scherer formula [22]. The estimated values of anatase A (004) and rutile R(101) grain size are $\sim 50 \text{ nm}$ and $\sim 130 \text{ nm}$ respectively. Since the A(004) peak has the highest intensity than R(110) phase, the rutile phase weight fraction $W_R(\%)$ was estimated by Spurr-Mayer's equation [15, 23]. It was found that the rutile phase fraction $W_R(\%)$ has an estimated value of $\sim 44 \text{ wt.}\%$. In addition, it should be noted that 10% error in the values of $W_R(\%)$ is anticipated as the anatase to rutile phase intensity ratio is relatively weak, which is absorbed and saturated by both the strong peaks of Pt(111) electrodes and the corundum substrate.

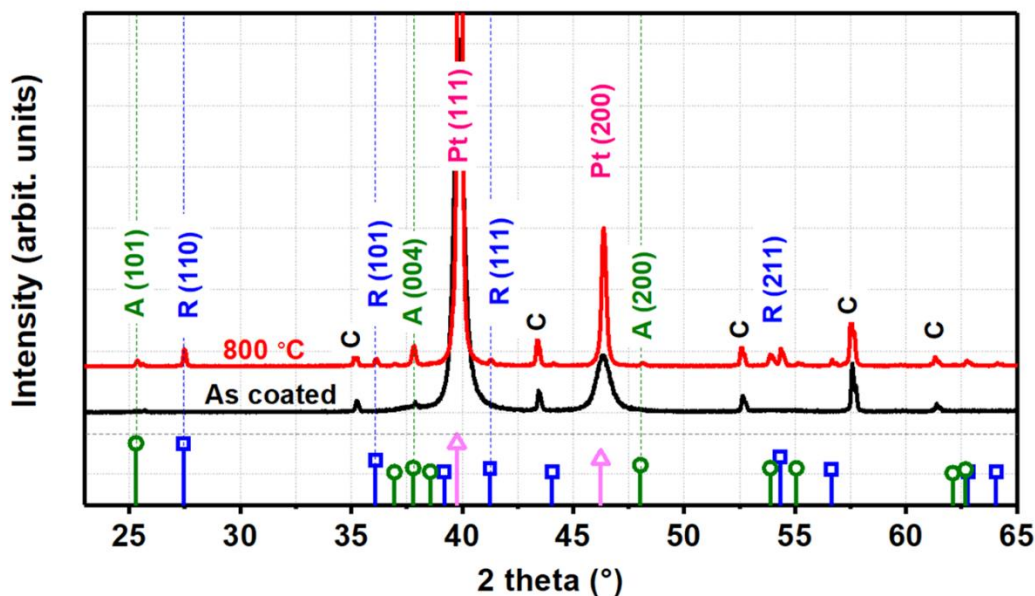


Figure 2. XRD patterns of as-deposited (AD), annealed (800°C) Pt/TiO₂/Pt samples, and JCPDS card.

In the present study, Pt has been used as a metallic bottom and top electrode because it has excellent adhesion with a corundum substrate, superior thermal and chemical stability under extreme conditions, high melting point (~1772°C), and oxidation resistance [24, 25]. Prior to the real sensor fabrication, the adhesion and high-temperature stability tests for Pt electrodes were performed. As aforementioned, the used parameters produced a ~200 nm thick Pt layer onto the substrate and TiO₂ surface as well. It is evident from **Fig. 3a-b** that both the bottom and top Pt layers yielded divergent surface morphologies due to the different underlying material types. This happens because Pt (and almost all metals) can develop diverse microstructures conforming to the crystal structure of substrate material [26]. No significant change in the physical appearance of both electrodes was observed after annealing at 800°C. Furthermore, the FE-SEM micrographs show that the Pt layer of the annealed sample is dense and has a larger crystal size. Since Pt has high atomic mobility, the change in the microstructure of the Pt layer caused by the annealing is most probably caused by the internal stress and the increase in the surface diffusion rate.

According to the FE-SEM micrographs of the prepared samples (**Fig. 3c,d**), the sensing layers are characterized by the surface with irregularly distributed micro-textured bumps (or nodules) with prismatic heads ranging in the size of ~1-2 μm and compactly packed sub-micrometer sized cracks separating the surface granulates. Upon close inspection of the enlarged view in **Fig. 3e,f** it can be seen that the annealing at 800°C has resulted in the densification of the sensing layer due

to the transformation of amorphous grains into the multi-faceted crystalline grains of anatase and rutile on the surface. Further, it is observable from the cross-sectional analysis in **Fig. 3g-j** that the sensing layers consist of $\sim 2 \mu\text{m}$ long vertically aligned micro-columns with very fine grains of the orders of several tens of nanometers. This corresponds to the typical quasi-feather-like micro-columnar structure with occasionally combined closely-packed grain structure. The structure has obvious columns (pillars) growing from the bottom Pt electrode to the top surface of the sensor and grain boundaries with clear voids. The annealing seems to have a pronounced effect on the micro-columnar structure. The grains along the micro-columns became denser and coarsened due to annealing in **Fig. 3j**. Each column seems to have granules elongated in the vertical direction that is analogous to the coarsened column which contained only a few faceted grains (size reaching 200 – 600 nm) with voids. There are spaces between the micro-columns of the sensing layers which widened significantly after annealing providing channels (marked as a red rectangle in **Fig. 3j**) for efficient H_2 adsorption and diffusion. It is worth noticing that there exist contradicting values of the grain size estimated using XRD and FE-SEM. The granulate values obtained from FE-SEM are higher than the crystallite size obtained from XRD. As the prepared TiO_2 sensing layers contain a large number of point defects and dislocations, the probable reason for such discrepancy is the fact that XRD values correlate to the size (or volume) of the coherent domain, thus the grain size values obtained by using FE-SEM analysis sound more accurate [27].

The elemental mapping analysis of each interface leverages the elemental composition and estimates the approximate at. % of Ti, O, Pt, and Al. The cross-sectional EDX analysis and element mapping of the samples in **Fig. 3k**, l show that the TiO_2 composition is close to chemically stoichiometric nearby the top surface and non-stoichiometric TiO_{2-x} adjacent to the bottom Pt electrode. In addition, for the annealed samples, it is worth mentioning that Pt diffuses several nanometers into the TiO_2 layer **Fig. 3l**, which can be caused by thermally induced inter-diffusion at 800°C . This intrigues that the bottom Pt/ TiO_2 is probably less Schottky than the top Pt/ TiO_2 interface. To confirm these results quantitatively, a more detailed GDOES analysis was carried out. The element distribution curves of the deposited Pt/ TiO_2 /Pt structure show that a strongly non-stoichiometric TiO_{2-x} layer is deposited near the BE interface. Near the top surface, in particular, very low Ti and higher oxygen concentrations than stoichiometric TiO_2 were measured, which indicates that when the TiO_2 layer is deposited, excess oxygen is adsorbed on the surface of the sensing layer. On the other hand, the elemental distribution of Ti and O in the annealed samples

remained constant over the entire layer, close to the stoichiometric Ti:O ratio (1: 2). However, the measured Ti:O ratio in the area adjacent to BE is very different and is estimated to be around 0.85:2.15, which indicates that the oxygen concentration gradient remained there even after heat treatment. The lower oxygen concentration of the TiO_2 layer in the vicinity of the bottom electrode leads to a strongly defective TiO_{2-x} layer containing a higher number of oxygen vacancies V_o^{2+} . A near stoichiometric ratio of 1:2 was observed from the depth profile analysis of the annealed sample. However, the interdiffusion at the bottom interface is probably more effective. The formation of non-stoichiometric TiO_{2-x} has already been explained in our previous report published elsewhere [15]. In addition, this effect was also confirmed from GDOES analysis that the annealing also rendered more Pt diffusion to the TiO_2 at the bottom electrode, see **Fig. 3m,n** and **Fig. S2** in the supplementary data.

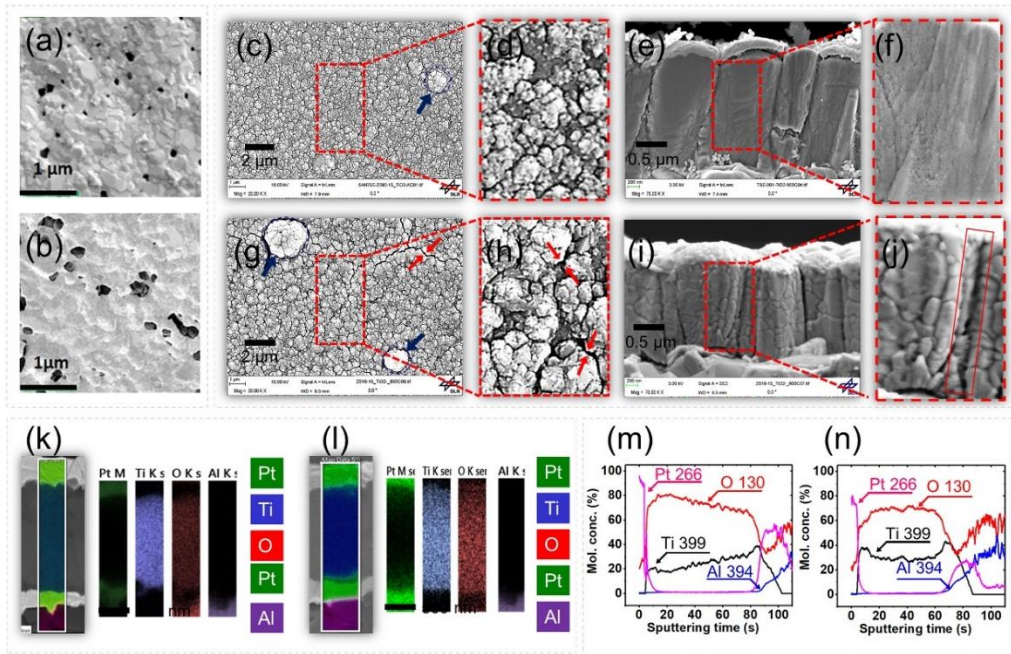


Figure 3. The figure shows the FE-SEM micrographs of the Pt-BE electrode deposited directly onto corundum substrate (a) and Pt-TE deposited on the TiO_2 top surface both annealed at 800°C (b), along with the surface and cross-sectional FE-SEM micrographs of as-deposited (c, e, g, i) and annealed (d, f, h, j) samples. The blue and red-colored arrows in the figure indicate the bumps/nodules and cracks on the surface respectively. The EDX elemental mapping (k, l) and GDOES analysis (m, n) of both the as-deposited and annealed samples are shown, respectively. The figure also shows FE-SEM micrographs with cross-sectional views (c, d) and (g, h). The black scale lines in FE-SEM micrographs (a, b), (c, d), (e, f, I, j), (g, h) and EDX mapping (k, l) indicate the $1\ \mu\text{m}$, $2\ \mu\text{m}$, $0.5\ \mu\text{m}$ and $0.5\ \mu\text{m}$ scale bar, respectively.

3.2 Sensor performance

To determine the sensor performance, one must estimate the following parameters very carefully: sensor response which is directly linked with the sensitivity, selectivity, response, and recovery times, power consumption, stability, linearity, resolution, and operating temperature. The sensor response (or response) in the current study is defined as the following ratio $S_R \sim R_{\text{air}}/R_{\text{H}_2}$ (R_{air} and R_{H_2} correspond to the saturated resistance value in air and specific H_2 concentration, respectively), the selectivity factor is defined as the ratio of the response of the sensor toward the target gas to the response of the sensor toward interfering gas ($S_F = S_{\text{RH}_2}/S_{\text{RX}}$; here S_{RX} is the sensor response to other gases CO , CO_2 , NO and NO_2), response and recovery times are estimated as the time taken by the sensor to reach 90% of the saturated value in H_2 gas and air respectively, and the remaining parameters were determined directly from the analysis. The prepared sensors showed excellent reproducible responses to increasing cyclic concentrations of H_2 gas even at room temperature, see **Fig. 4a-c**. To commence with, we initially carefully observed the resistance values of the sensors in the air at the specific operating temperature. According to the general perception, TiO_2 films are highly resistive under oxidizing environments ($R_{\text{air}} \geq 10^{12} \Omega$) thus minute changes in the resistance upon H_2 exposure are even unnoticeable. In our case, however, the resistance of the annealed sample in the air is relatively lower $1.39 \times 10^{10} \Omega$ at RT, $229 \times 10^9 \Omega$ at 50°C , $1.203 \times 10^8 \Omega$ at 100°C , see **Fig. 4d**. The probable reasons for the lower resistance are as follows: (i) TiO_2 in the present study are composed of quasi-feather like structure offering channels for the efficient gas adsorption, (ii) the annealing has caused sufficient Pt into the TiO_2 layers thus significantly reducing the Schottky barrier height and (iii) as the thickness of the TiO_2 is $\sim 2 \mu\text{m}$ which thereby reduces the electrode spacing.

It is noticeable from **Fig. 4a-c** that the annealed sensors show a rapid response of four orders of magnitude at RT that increases linearly with increasing H_2 concentrations having a good correlation factor improving with increasing operating temperature, the estimated values are $R^2 \sim 0.82$ at RT, $R^2 \sim 0.88$ at 50°C and $R^2 \sim 0.99$ at 100°C , see **Fig. 4e**. To be more specific, the calculated values of the sensor response toward 10000 ppm H_2 are $S_R \sim 2.86 \times 10^4$, $\sim 1.50 \times 10^5$ and $\sim 1.95 \times 10^6$ at RT, 50°C and 100°C respectively. Despite our gas sensor setup being limited to 300 ppm as the lowest possible H_2 concentration, it can be seen that the sensors also exhibited a good

response to lower H₂ concentrations. For instance, for 300 ppm the response values of the sensors are S_R ~16, ~34, and ~345 at RT, 50 °C, and 100 °C respectively. Then the selectivity of the sensors was checked and elaborated in **Fig. S3**. It was found that the sensors are highly selective to H₂ against other interfering gases such as CO, CO₂, NO, and NO₂. The sensors showed high values of selectivity factor, for example at RT toward 1000 ppm of other gases the selectivity factor was approximately the same as the sensor response in 1000 ppm H₂ ($S_F \cong S_{RH_2} \cong 3584$).

Further selectivity analysis revealed the sensor response is limited to only a specific range of interfering gases concentration, while toward H₂ the detection range is wide (300 – 10000 ppm). Since the sensor response values are not yet saturated at lower (300 ppm) or higher H₂ concentrations (10000 ppm), thus indicating further expected expansion of the lower and higher detection limit of our sensors, thus an excellent resolution of the sensor is anticipated. The high selectivity can be attributed to the fact that H₂ molecules can easily diffuse through the porous top Pt electrode and interact with the TiO₂ surface. Additionally, the Pt electrode can also act as a catalyst to enhance the reaction between H₂ and TiO₂, which is not the case with other gases such as CO, CO₂, NO, and NO₂ that have more electronegative atoms (such as oxygen and nitrogen), which prefer to attract and hold onto electrons rather than donate them. As a result, the response of the sensor to these gases is relatively weak compared to H₂ [15, 18].

Fig. 4f illustrates the reaction time estimation procedure, where at RT the estimated T_{res} ~45 s and T_{rec} ~165 s are mentioned toward 5000 and 10000 ppm H₂. The response time values in **Fig. 4g** are of the order of tens of seconds at RT which become more rapid at 50 °C and 100 °C, i.e., T_{res} [in seconds] ~156-43 at RT, 81-20 at 50 °C and 64-15 at 100 °C. While the recovery time values in **Fig. 4h** gradually increase with increasing H₂ concentration but decrease with increasing temperature i.e., T_{rec} [in seconds] ~116-228 at RT, 100-200 at 50°C and 56-108 at 100 °C. It is anticipated that the reaction time values are influenced by the experimental setup such as the gas mixing procedure [15, 20, 28, 29].

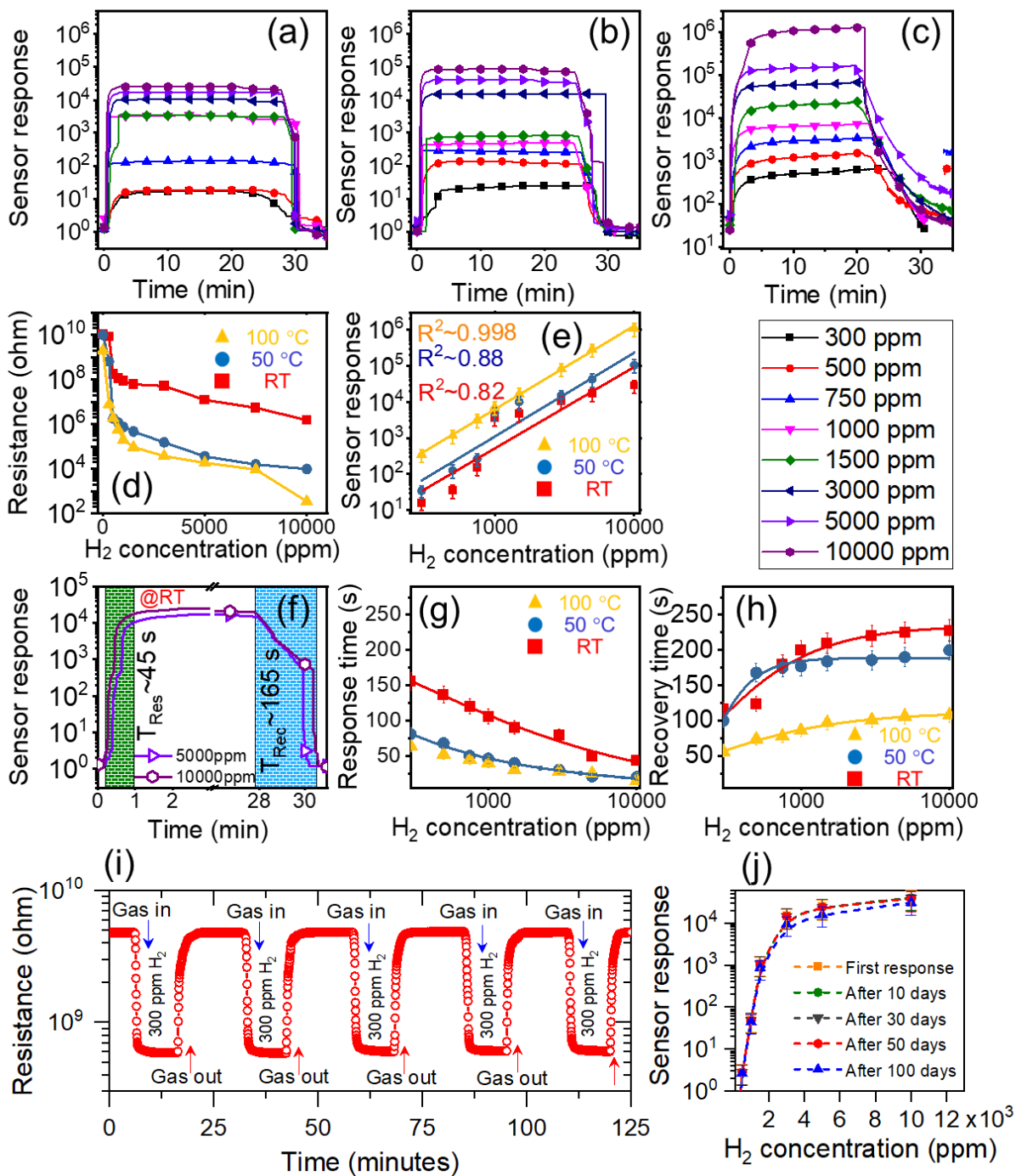


Figure 4. Dynamic responses of 800°C annealed sensors to different H₂ concentrations at room temperature (a), 50°C (b), and 100°C (c). The legend on the lower right is of (a), (b), and (c). The sensor responses (d) and resistance (e) versus H₂ gas concentrations graphs, the graphs showing the estimation of response and recovery time's values (f) and the graphs of response (g) and recovery times versus H₂ concentrations (h) are plotted, the repeatability (or reproducibility) test of the sensor for 5 consecutive cycles to 300 ppm at room temperature (i)

and long-term stability test to various concentrations 300 – 10000 ppm H₂ is shown in (j); here $\times 10^3$ indicates the concentrations in thousands of ppm.

Further, the stability tests (both short-term and long-term) were performed. **Fig. 4i** shows the short-term stability test or also known as repeatability/reproducibility of the sensor toward 300 ppm at room temperature and it is evident that the sensor response is reproducible and repeatable. It is also concluded from **Fig. 4j** that the sensor showed excellent long-term stability over 100 days. The response is slightly decreased after 100 days most probably due to the weather change during this time, however, overall the sensor response is highly stable. Since the operating temperature of the sensors is RT, which means no resistive heater is required. In addition, with the applied voltage of 1.0 V, so typically such a sensor can only consume about $\sim 10^{-9}$ Watts of power. The results obtained in the study are compared with previous literature data, see Table S1 in the supplementary data.

Basically, the hydrogen sensing mechanism on a Pt/TiO₂/Pt structure strongly depends on the presence of a depletion layer due to the chemisorption of oxygen on the surface of TiO₂ which is an n-type semiconductor. This depletion layer affects the resistance of the metal oxide and contributes to the sensing response. After the Pt/TiO₂/Pt structure is exposed to hydrogen gas, the hydrogen molecules adsorb onto the Pt nanoparticles supported on the TiO₂ surface [17]. This process leads to the dissociation of hydrogen molecules into hydrogen atoms. It is also well established that the hydrogen atoms diffuse through the top Pt surface and reach the TiO₂ surface, where they interact with the chemisorbed oxygen species. In the absence of hydrogen gas, the chemisorbed oxygen species contribute to the formation of a depletion layer in the TiO₂ material, which results in increased resistance of the sensor [18]. In fact, this depletion layer acts as a barrier to the flow of electrical current. However, under the hydrogen gas exposure, the hydrogen atoms react with the chemisorbed oxygen species on the TiO₂ surface. This reaction reduces the amount of chemisorbed oxygen, leading to a decrease in the thickness of the depletion layer. As a result, the resistance of the Pt/TiO₂/Pt structure decreases, which is in good agreement with previous reports [20, 27]. The change in resistance induced by the reaction of reducing gases, such as hydrogen, mainly results from their interaction with the chemisorbed oxygen species. The reduction of the chemisorbed oxygen decreases the thickness of the depletion layer and, consequently, reduces the resistance of the metal oxide. By measuring the change in resistance of the Pt/TiO₂/Pt structure, it becomes possible to detect the presence of hydrogen gas. The decrease in resistance indicates the occurrence of the reaction between hydrogen and the chemisorbed oxygen, providing a reliable sensing signal for the detection of hydrogen [27].

3.3 Discussion on H₂ reaction kinetics

It is evident from the above-mentioned sensor performance that the Pt/TiO₂/Pt system has rendered a humungous response ($\sim 10^6$ orders of magnitude at 100°C) toward 10,000 ppm H₂. Even at room temperature, an excellent response of $\sim 10^4$ was achieved, which was not possible with the conventional sensors design configurations using standard interdigitated comb-like electrode systems (IDEs). Furthermore, the reaction times are fast, thus suggesting rapid adsorption, accumulation, and subsequent diffusion of hydrogen ions onto the Pt/TiO₂/Pt system. For this reason, we plotted the comparative dynamic responses of the sensor with top and bottom electrode structure (Pt/TiO₂/Pt) and classical interdigitated electrodes structure (IDEs) in **Fig. S4**: it is worth mentioning that the IDEs-based sensors did not show any response at RT, 50°C and 100°C. This figure is a complete guide to understanding the difference between the adsorption reactions of the two mentioned sensors. It can be noticed that Pt/TiO₂/Pt response rising curves toward various H₂ concentrations show the decreased value of the slope magnitude. Therefore, the response and recovery times are faster for Pt/TiO₂/Pt type sensors than sensors with IDEs structures. However, while designing a gas sensor one must also consider the adsorption kinetics as one of the utmost parameters because it helps to gain more scientific insights to unravel the adsorption rates at which gas molecules react with the sensing layer surface. Therefore, it is of utmost importance to develop an understanding of gas sensor kinetic reactions which are significantly influenced by the complexity of the gas sensing layer surface as well as its reaction with various gas concentrations. It is anticipated that the most important models to prognosticate the gas adsorption reaction onto the sensing layer surface are Elovich reactions, inter-particle diffusion (IPD), pseudo-first-order (PFO), and pseudo-second-order (PSO). Recently it has been proved recently that PFO and PSO models best describe the hydrogen adsorption kinetics onto ordered mesoporous TiO₂ system [30]. In addition, to estimate the reaction rates, the appropriateness of the model is also solely subject to the precision level (or error parameter), i.e., the R² values (correlation coefficient) obtained after the fitting that shows the errors in the fitting. To begin with the modeling of the sensor responses, the following presumptions are made:

1. The fast H₂ molecule adsorption process onto the Pt surface is primarily dissociative chemisorption.

2. The free hydrogen atoms form a close tie and establish a chemical bond onto the TiO₂ surface (refer to as subsurface adsorption) after hitting the top Pt electrode; the concept of the subsurface is used here to distinguish it from the real surface of TiO₂, because TiO₂ surface is covered by Pt and H₂ molecules do not directly adsorb onto TiO₂.
3. Subsequently, the hydrogen accumulation onto the subsurface and penetration to the bulk may trap vacant adsorption sites arising from the surface and bulk defects.
4. The ionic conduction channels arise due to the ionic defects such as $V_o^{\bullet\bullet}$ and $T_i^{\bullet\bullet\bullet\bullet}$ within the TiO₂ matrix. However, electronic conduction in n-type TiO₂ is predominant under the oxygen environment, while ionic conduction channels might become wider under the H₂ environment.
5. Thus the measured value of the resistance is not purely electronic nature but rather a combination of electronic as well as ionic nature.

Based on the aforementioned assumptions and the obtained results, we attempted to gain more fundamental insights by comparing experimental data to theoretical models by using four basic adsorption models, namely, i) the Elovich reaction model, (ii) the inter-particle diffusion (IPD) model, (iii) pseudo-first-order (Lagergren's first order – PFO) and (iv) pseudo-second-order (Ho's model – PSO) [24, 31-35]. There have been several attempts made to improve the fitting by modifying the raw data and mathematical treatments, but that ingenerate further complexities of underlying adsorption because there exist distinctive processes during the whole adsorption process. Particularly, in our present case, the adsorption process is swift, thus the probability of adjusting the parameter, t (time) with built-in functions is relatively low [33, 34]. On that account, we directly employed the differential equations of Elovich, IPD, and PFO models to fit our experimental dynamic curves to avoid any further complications. While for the PSO model, the experimental data were fitted linearly to extract the constants and the surface coverage. Hence, we believe that the estimated parameter values obtained this way are more accurate with both used techniques in this work. Furthermore, after careful analysis, we found that Elovich and IPD models did not fit our experimental data as well as the PFO and PSO models. While the Elovich and IPD models are still valid and have been widely used in adsorption studies, we believe that including them in the main text would distract from the focus of our study and could potentially confuse readers. As such, we have included the data and analysis of these models in the supplementary

information for interested readers. The Elovich and IDP and PFO fitting curves are shown in **Fig. 5a,b** and the obtained parameters are shown in **Table S1**.

Table 1. The estimated values and experimental data of the parameters were obtained by fitting of PFO model.

C_{H_2} (ppm)	Pseudo first-order model								
	Room Temperature			50°C			100°C		
	R^2	k_2	θ_e	R^2	k_2	θ_e	R^2	k_2	θ_e
300	0.98208	0.00549	17.8297	0.89241	0.00239	19.37595	0.99718	0.00654	31.46601
500	0.96288	0.00703	18.76809	0.94881	0.00692	25.25587	0.98016	0.00739	146.3982
750	0.86259	0.02029	133.2588	0.74912	0.02493	57.858	0.99769	0.00665	286.6435
1000	0.81011	0.02107	3271.992	0.7827	0.01757	152.5032	0.9966	0.01042	2947.893
1500	0.75547	0.00574	3842.021	0.78846	0.00819	612.1717	0.95579	0.00492	7947.786
3000	0.86286	0.01196	10708.38	0.90144	0.01454	1428.932	0.98449	0.01105	15336.06
5000	0.90718	0.015	17220.21	0.9048	0.01436	2375.885	0.97732	0.00879	40953.9
10000	0.17239	0.0181	25403.29	0.27737	0.01668	68964.63	0.80654	0.001384	87229.06

It is generally accepted that the adsorption reaction kinetics under the nonequilibrium conditions can be best fitted by using the first-ordered reaction kinetics (Lagergren adsorption reaction) and second-order rate equation. Generally, the adsorption process is regarded as a reversible reaction, which is also true in H₂ adsorption onto the Pt/TiO₂/Pt system. The first-order adsorption kinetics are expressed by using Equation (1) [31, 35- 38].

$$\frac{d\theta_t}{dt} \cong k_2 (\theta_e - \theta_t) \quad (1)$$

Where k_2 , θ_e , and θ_t are first-order reaction rate constant, the surface coverage of hydrogen on Pt/TiO₂/Pt system at equilibrium and period of actual time (dynamic θ at any time t) respectively. The hydrogen surface coverage θ_e , and θ_t are both directly related to the saturated sensor resistance under gas exposure (R_{gas}) and dynamic sensor resistance at any time t. Integration of equation (1) yields the following relationship in Equations (2), (3), and (4):

$$\ln(\theta_e - \theta_t) = \ln(\theta_e) - k_2 t \quad (2)$$

Upon further simplification, we can write:

$$\ln[1 - (\theta_t/\theta_e)] = -k_2 t \quad (3)$$

Alternatively, the above equation can be written as:

$$\theta_t \cong \theta_e [1 - \exp(-k_2 t)] \quad (4)$$

The fitting of the plots of S_R against time (see **Fig. 5c**) resulted in the estimation of equation constants rate constants k_2 , θ_e , and θ_t with significant variation. However, the rate constants ($k_2 \cong 0.00549$ - 0.0181 at RT, $k_2 \cong 0.00239$ - 0.01668 at 50 °C and $k_2 \cong 0.00654$ - 0.01384 at 100 °C) and equilibrium the adsorption capacity ($\theta_e \cong 17.82$ - 25403.29 at RT, $\theta_e \cong 19.37$ - 68964.63 at 50 °C and $\theta_e \cong 31.46$ - 87229.06 at 100 °C) seems to have logical values as expected because these values increase with increasing H₂ concentration and operating temperature (see **Table 1**). Despite improved trends observed for the estimated PFO model constants, the above data seems to provide insufficient evidence for the fitting to be called perfectly linear because the R-square values are in the range of 0.172-0.98 at RT, 0.27-0.94 at 50 °C and 0.80-0.99 at 100 °C. The disparity of the

obtained data at RT and 50 °C is higher, while the order of the estimated data with PFO is an improved sequence.

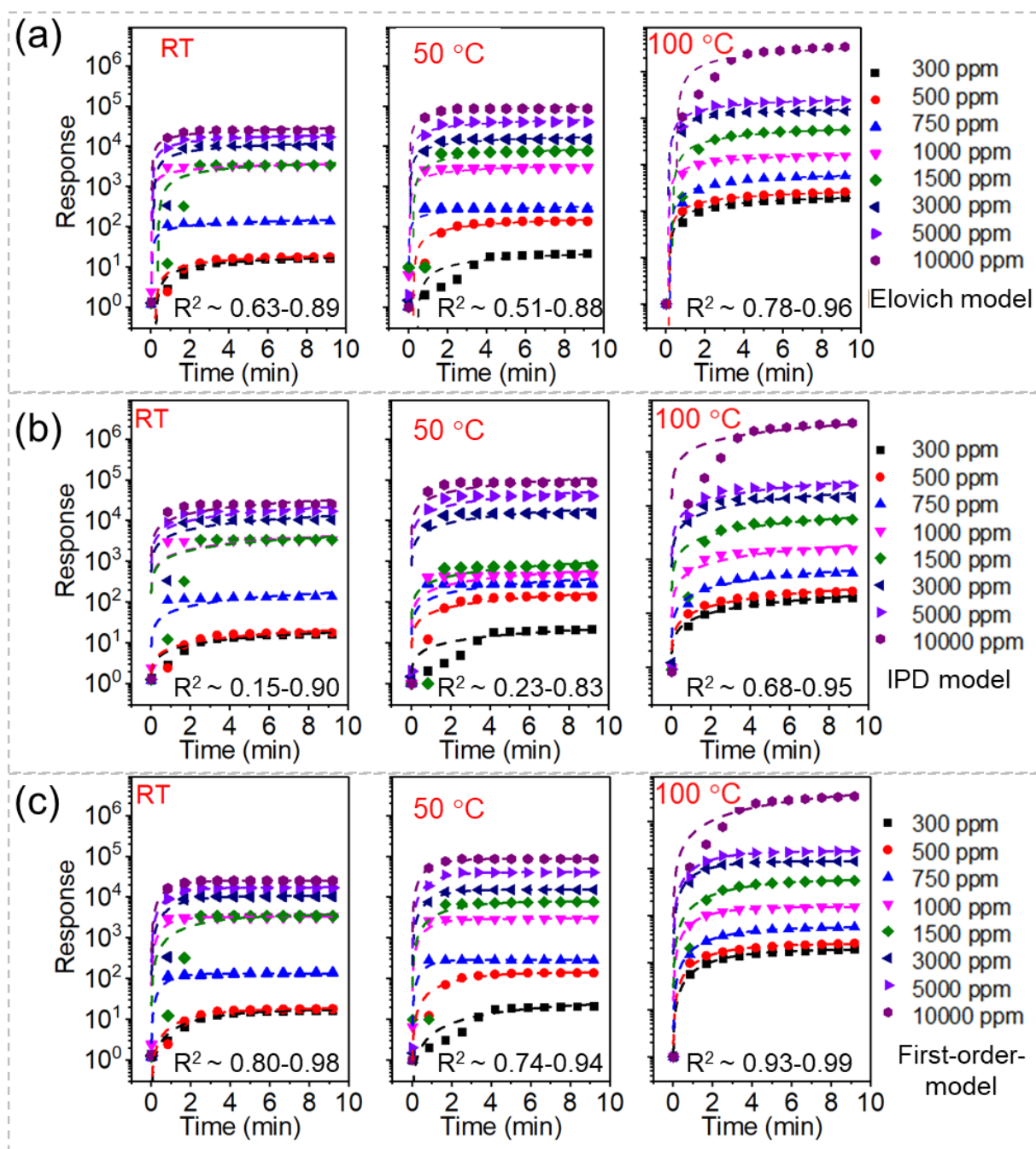


Figure 5. The response and regression analysis of H₂ adsorption (300 – 10,000 ppm) on Pt/TiO₂/Pt surface. The original data (various color symbols) and its fitting (various color dashed lines) by Elovich model (a), Inter-particle diffusion model (b), and pseudo-first-order model (also known as Lagergren’s first order model) (c).

Several mathematical relationships are proposed to describe the pseudo-second-order (PSO) adsorption kinetics. Based on the CO₂ sorption capacity of a solid material (platinum electrode), the first attempt to delineate PSO was put forward by Sobkowski and Czerwinski in 1974 (SC-PSO). This was then followed by a series of investigations (both theoretical and experimental) by Ritchie in 1977 (R-PSO), Blanchard in 1984 (B-PSO), and Ho in 1995 (Ho-PSO). Ritchie's PSO model (R-PSO) was applied to the adsorption of gases onto solid surfaces and also for some solution/solid sorption systems [39-42]. Meanwhile, the Blanchard model (B-PSO) was used mostly to understand the exchange kinetics of heavy metal ions on the solids (such as zeolites) by assuming that the adsorption and desorption reaction solely charge the complete sorption process. The latest and simplest PSO model was predicted by Ho (Ho-PSO), which also included the chemisorption of gases onto solid material surfaces. In our latest studies, we found that Ho's PSO model can directly describe the room temperature H₂ adsorption reactions onto the ordered mesoporous TiO₂ with high accuracy (R²-values > 0.99). While we only included the Ho-PSO model in the main manuscript due to its best fitting, other models (SC-PSO, R-PSO, and B-PSO models) are discussed in the supplementary data.

A pseudo-second-order model was presented by Ho and McKay [43, 44, 45], which fits exceptionally well for the adsorption of metallic species (divalent metals) during agitation onto solid surfaces (sphagnum moss peat). The model is based on the assumption that the kinetic reaction is second order and it mainly involves the chemisorption between divalent metal and peat, this happens because the covalent forces originate due to the sharing (or exchange) of electrons. Given that the concentration gradient ($q_e - q_t$) is the driving force for the reaction kinetics and directly proportional to the number of active available adsorption sites. Here q_t and q_e are the number of divalent metal ions adsorbed on the surface of peat at any time t and equilibrium respectively. Considering, k is the rate constant then the second-order rate kinetics can be written as follows:

$$\frac{dq_t}{dt} = k (q_e - q_t)^2 \quad (5)$$

The linear form of Ho's PSO model can be obtained by integrating equation (5) for the given boundary conditions ($q_t=0 - q_t$ at time $t=0 - t$) as follows, see equation (6) [26, 46, 47]:

$$\frac{t}{q_t} = \frac{1}{kq_e^2} + \frac{1}{q_e}t \quad (6)$$

Here the constant kq_e^2 is the initial adsorption rate. To synchronize the obtained parameters, the above equation is compatible with our assumed constants as follows in equation (7):

$$\frac{t}{\theta_t} = \frac{1}{k_3\theta_e^2} + \frac{1}{\theta_e}t \quad (7)$$

For this model, the rate constants can be obtained by plotting $\frac{t}{\theta_t}$ against t , where θ_t is consistent with the dynamic sensor response (S_R at time t) and saturated value of S_R in the respective concentration of H_2 gas (see **Fig. 6**).

The fitting of the experimental data with the H-PSO model is shown in **Fig. 7** and the obtained parameters are given in **Table 2**. Upon close inspection of the fitting curves, the obtained data make it possible to determine that the H-PSO model has the highest accuracy among all other aforementioned models. The calculated values of the coefficients of determination are rather high ($R^2 \cong 0.981 - 0.999$ at RT, $0.978 - 0.999$ at 50°C and $0.975 - 0.998$ at 100°C), which indicates the highest appositeness of the H-PSO kinetic model to best describe the H_2 adsorption on Pt/TiO₂/Pt system temperature from RT to 100°C . The values of rate constants k ($k \cong 0.98 - 0.999$ at RT, $0.978 - 0.999$ at 50°C and $0.975 - 0.998$ at 100°C) and adsorption capacity at equilibrium ($\theta_e \cong 2.54 \times 10^8 - 2.78 \times 10^5$ at RT, $4.17 \times 10^7 - 5.04 \times 10^4$ at 50°C and $1.88 \times 10^6 - 5.70 \times 10^2$ at 100°C) are significantly pertinence with the experimentally obtained values of sensor response and saturated resistance values in respective H_2 gas as shown in **Fig.7**.

Table 2. The estimated values and experimental data of the parameters obtained by fitting of Ho's equations.

C_{H_2} (ppm)	Second order (Ho's) Model									Experimental data						
	Room Temperature (RT)			50°C			100°C			RT		50°C		100°C		
	R^2	κ_3	θ_ε	R^2	κ_2	θ_ε	R^2	κ_2	θ_ε	S_R	R_{gas}	S_R	R_{gas}	S_R	R_{gas}	
300	0.994	1.77E+01	2.54E+08	0.978	2.92E+01	4.17E+07	0.993	3.42E+02	1.88E+06	1.60E+01	2.23E+08	3.44E+01	2.19E+07	3.44E+01	1.84E+06	
500	0.997	2.37E+01	1.60E+07	0.996	1.28E+02	1.69E+06	0.993	1.15E+03	3.67E+05	3.50E+01	1.15E+08	1.26E+02	1.18E+07	1.26E+02	5.05E+05	
750	0.999	2.97E+02	3.11E+07	0.999	3.69E+02	3.50E+06	0.995	3.06E+03	1.65E+05	1.52E+02	3.32E+07	2.63E+02	3.59E+06	2.63E+02	1.99E+05	
1000	0.999	1.49E+03	2.90E+07	0.998	5.09E+03	2.11E+06	0.998	7.19E+03	6.13E+05	3.58E+03	1.88E+07	4.92E+03	1.84E+06	4.92E+03	8.31E+05	
1500	0.981	4.58E+03	1.66E+07	0.994	1.21E+04	1.20E+06	0.993	1.71E+04	5.21E+05	4.65E+03	1.24E+07	1.00E+04	1.10E+06	1.00E+04	4.24E+05	
3000	0.997	1.05E+04	9.23E+06	0.998	1.57E+04	8.43E+05	0.998	8.27E+04	2.22E+05	1.03E+04	1.06E+07	1.50E+04	9.22E+06	1.50E+04	1.76E+05	
5000	0.998	1.55E+04	8.72E+06	0.998	4.50E+04	5.41E+05	0.997	2.51E+05	1.03E+05	1.73E+04	9.67E+06	4.25E+04	6.40E+06	4.25E+04	9.97E+05	
10000	0.999	2.78E+05	8.08E+06	0.999	1.06E+06	5.04E+05	0.975	1.15E+07	5.70E+05	2.86E+04	7.82E+06	1.05E+05	4.70E+06	1.05E+05	4.06E+05	
	00	35	05	06	35	05	04	46	06	02	04	06	05	04	05	02

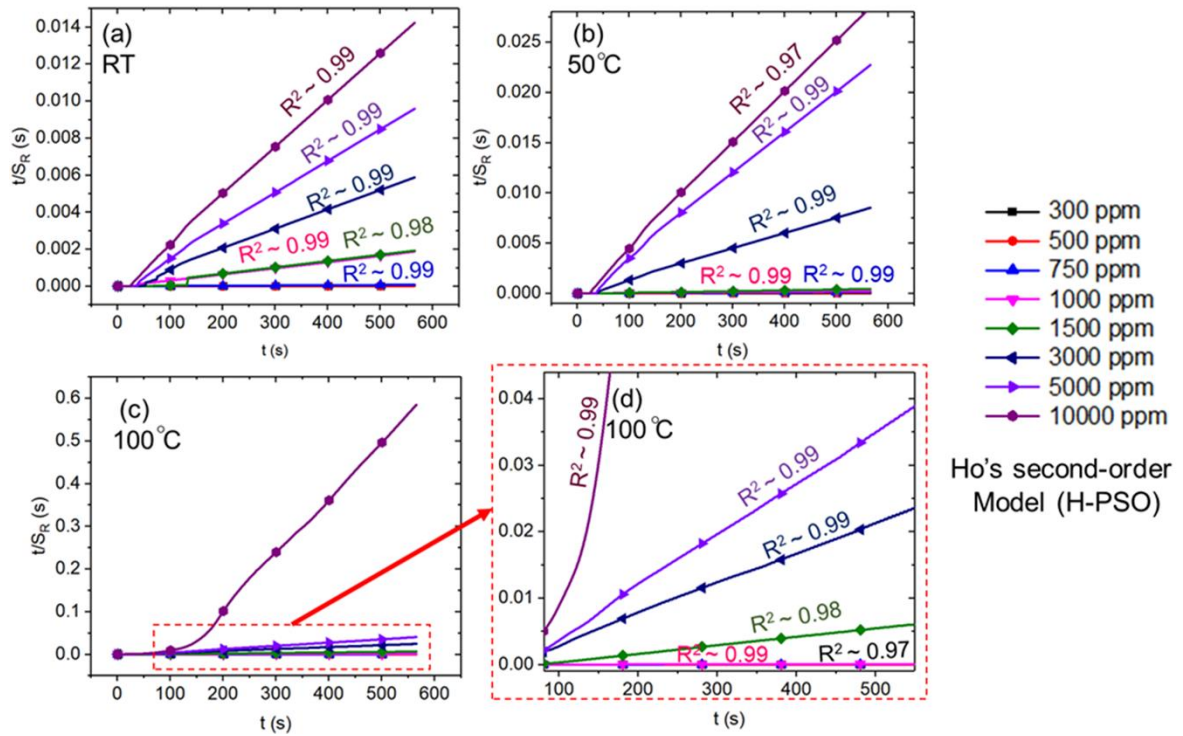


Figure 6. The response and regression analysis of H_2 adsorption (300 – 10,000 ppm) on Pt/TiO₂/Pt surface via pseudo-second order Ho's model at RT (a), 50°C (b) and 100°C (c, d)

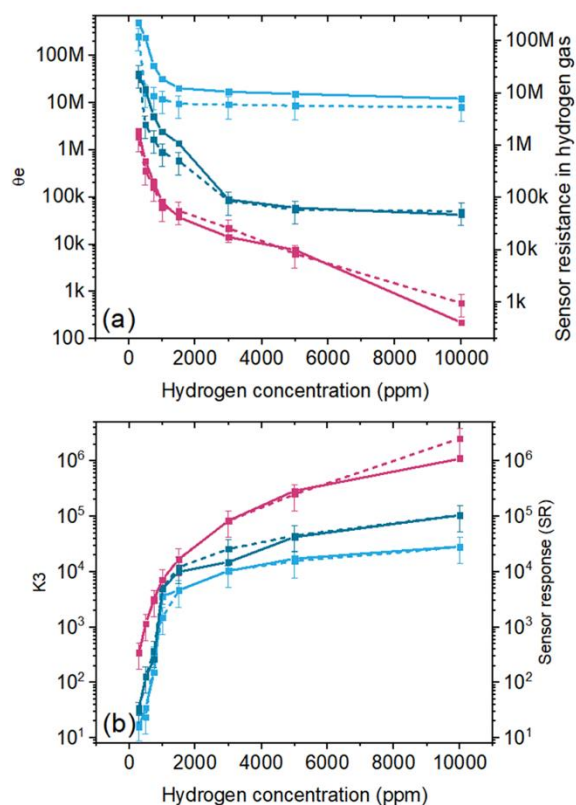


Figure 7. The comparative plots showing the compatibility of experimental data and parameters obtained from the fitting of Ho's PSO model

4. Conclusions

Highly sensitive hydrogen gas sensors based on Pt/TiO₂/Pt structure have been successfully prepared. The XRD diffractograms confirm the predominance of unanticipated anatase A(004) peak over anatase A(101) and rutile R(110) peaks, intriguing the quasi-preferential orientation of the TiO₂ sensing layer. The SEM, EDS, and GDOES analysis confirmed the presence of a typical columnar structure of the sensing films and a higher diffusion rate at the bottom Pt/TiO₂ interface. The sensor response S_R at room temperature is relatively high for all tested H₂ concentrations (e.g., $S_R \sim 2.86 \times 10^4$ toward 1000 ppm H₂) with a response T_{res} and recovery T_{rec} time of ~ 43 s and ~ 228 s respectively. The H₂ selectivity factor of the sensor is $SF \sim 3584$ against other interfering gases (e.g., 1000 ppm of CO, CO₂, NO, and NO₂) and the power consumption is $\sim 1 \times 10^{-9}$ W. The values of S_R , T_{res} , and T_{rec} further improved progressively with the increasing the operating temperature

of the sensor (e.g., $S_R \sim 1.50 \times 10^5$ and $\sim 1.95 \times 10^6$, $T_{res} \sim 20$ s and 15 s, $T_{rec} \sim 200$ s and 108 s toward 10000 ppm H_2 at 50°C and 100°C). After fitting the data with various adsorption models, it was found that Ho's pseudo-second-order model (H-PSO) best describes the adsorption kinetics of the sensor responses at all operating temperatures with excellent linearity $R^2 \cong 0.981 - 0.999$. The obtained parameters of H-PSO models are well in agreement with the experimental data (e.g., $k \cong 1.77 \times 10^1$ and 2.78×10^5 correspond to $S_R \cong 1.60 \times 10^1$ and 2.86×10^4 , $\theta_e \cong 2.54 \times 10^8$ and 8.08×10^6 correspond to $R_{H_2} \cong 2.23 \times 10^8$ and 7.82×10^6 toward 100 and 10000 ppm H_2 at RT).

Author contributions

Azhar Ali Haidry: Conceptualization, Methodology, Original Manuscript Writing, Formal Analysis, Investigation, Project Administration. **Yinwen Ji:** Methodology, Data Curation, Writing-Review and Editing. **Adil Raza:** Formal Analysis, Writing - Review and Editing. **Hao Zhu:** Data Curation, Visualization. **Ali Zavabeti:** Data curation, Formal analysis. **Bilge Saruhan:** Supervision, Funding Acquisition, Writing Review and Editing.

Conflicts of interest

The authors declare that they have no known competing financial interests or personal relationships that could have appeared to influence the work reported in this paper.

Acknowledgments

This work received financial support from the National Natural Science Foundation of China [grant numbers 51850410506]; and the Central University Basic Scientific Research Business Expenses Special Funds [grant numbers NG2020002].

References

- [1] H.S Gu, Z. Wang, Y.M Hu, Hydrogen gas sensors based on semiconductor oxide nanostructures, *Sensors*. 12(5) (2012) 5517-55550. <https://doi.org/10.3390/s120505517>.
- [2] X.Y. Zhou, T.Y. Tao, Y.W. Bao, X.H. Xia, K. Homewood, Z. Wang, M. Lourenço, Z.B. Huang, G.S. Shao, Y. Gao, Dynamic Reaction Mechanism of P-N-Switched H₂-Sensing Performance on a Pt-Decorated TiO₂ Surface, *Applied Materials and Interfaces*. 13(2021) 25472-25482. <https://doi.org/10.1021/acsami.1c02050>
- [3] K.G. Nair, V. Ramakrishnan, R. Unnathpadi, K.K. Karuppanan, B. Pullithadathil, Unraveling Hydrogen Adsorption Kinetics of Bimetallic Au–Pt Nanoisland-Functionalized Carbon Nanofibers for Room-Temperature Gas Sensor Applications, *The Journal of Physical Chemistry C*. 124(13) (2020) 7144-7155. <https://doi.org/10.1021/acs.jpcc.9b11147>.
- [4] C. Wadell, F.A.A Nugroho, E. Lidstrom, B. Iandolo, J.B. Wagner, C. Langhammer, Hysteresis-free nanoplasmonic Pd-Au alloy hydrogen sensors, *Nano Letters*. 15(5) (2015) 3563-3570. <https://doi.org/10.1021/acs.nanolett.5b01053>.
- [5] T. Hübert, L. Boon-Brett, V. Palmisano, M.A. Bader, Developments in gas sensor technology for hydrogen safety, *International Journal of Hydrogen Energy*. 39(35) (2014) 20474-20483. <https://doi.org/10.1016/j.ijhydene.2014.05.042>.
- [6] R. Ab Kadir, W. Zhang, Y.C Wang, J.Z. Ou, W. Wlodarski, A.P. O'Mullane, G. Bryant, M. Taylor, K. Kalantar-zadeh, Anodized nanoporous WO₃Schottky contact structures for hydrogen and ethanol sensing, *Journal of Materials Chemistry A*. 3 (2015) 7994-8001. <https://doi.org/10.1039/c4ta06286h>.
- [7] S. Phanichphant, Semiconductor Metal Oxides as Hydrogen Gas Sensors, *Procedia Engineering*. 87 (2014) 795-802. <https://doi.org/10.1016/j.proeng.2014.11.677>.
- [8] M. Vidiš, I.O. Shpetnyi, T. Roch, L. Satrapinsky, M. Patrnčiak, A. Plecenik, T. Plecenik, Flexible hydrogen gas sensor based on a capacitor-like Pt/TiO₂/Pt structure on polyimide foil, *International Journal of Hydrogen Energy*, 46(36) (2021), 19217-19228. <https://doi.org/10.1016/j.ijhydene.2021.03.052>
- [9] Z. Li, D. Ding, C. Ning, p-Type hydrogen sensing with Al- and V-doped TiO₂ nanostructures, *Nanoscale Research Letters*. 8(1) (2013) 1-8. <https://doi.org/10.1186/1556-276X-8-25>.

- [10] Z. Li, A.A. Haidry, T. Wang, Z.J. Yao, Low-cost fabrication of highly sensitive room temperature hydrogen sensor based on ordered mesoporous Co-doped TiO₂ structure, *Applied Physics Letters*. 111(3) (2017) 032104. <https://doi.org/10.1063/1.4994155>.
- [11] J.A. Woo, D.T. Phan, Y.W. Jung, K.J. Jeon, Fast response of hydrogen sensor using palladium nanocube-TiO₂ nanofiber composites, *International Journal of Hydrogen Energy*. 42(29) (2017) 18754-18761. <https://doi.org/10.1016/j.ijhydene.2017.04.189>.
- [12] O. Alev, A. Kilic, C. Cakirlar, S. Buyukkose, Z.Z. Ozturk, Gas Sensing Properties of p-Co(3)O(4)/n-TiO(2) Nanotube Heterostructures, *Sensors*. 18(4) (2018) 956. <https://doi.org/10.3390/s18040956>.
- [13] S.M. Kim, H.J. Kim, H.J. Jung, J.Y. Park, T.J. Seok, Y.H. Choa, T.J. Park, S.W. Lee, High-performance, transparent thin film hydrogen gas sensor using 2D electron gas at interface of oxide thin film heterostructure grown by atomic layer deposition, *Advanced Functional Materials*. 29(7) (2019) 1807760. <https://doi.org/10.1002/adfm.201807760>
- [14] O. Alev, E. Şennik, Z.Z. Öztürk, Improved gas sensing performance of p-copper oxide thin film/n-TiO₂ nanotubes heterostructure, *Journal of Alloys and Compounds*. 749 (2018) 221-228. <https://doi.org/10.1016/j.jallcom.2018.03.268>.
- [15] A.A. Haidry, A. E-Stahl, B. Saruhan, Effect of Pt/TiO₂ interface on room temperature hydrogen sensing performance of memristor type Pt/TiO₂/Pt structure, *Sensors and Actuators B: Chemical*. 253 (2017) 1043-1054. <https://doi.org/10.1016/j.snb.2017.06.159>.
- [16] W.P. Chen, Y. Xiong, Y.S. Li, P. Cui, S.S. Guo, W. Chen, Z.L. Tang, Z.J. Yan, Z.Y. Zhang, Extraordinary room-temperature hydrogen sensing capabilities of porous bulk Pt-TiO₂ nanocomposite ceramics, *International Journal of Hydrogen Energy*. 41(4) (2016) 3307-3312. <https://doi.org/10.1016/j.ijhydene.2015.12.151>.
- [17] H. Kwon, Y. Lee, S. Hwang, J.K. Kim, Highly-sensitive H₂ sensor operating at room temperature using Pt/TiO₂ nanoscale Schottky contacts, *Sensors and Actuators B: Chemical*. 241 (2017) 985-992. <https://doi.org/10.1016/j.snb.2016.11.022>.
- [18] T. Plecenik, M. Moško, A.A. Haidry, P. Ďurina, M. Truchlý, B. Grančič, M. Gregor, T. Roch, L. Satrapinsky, A. Mošková, M. Mikula, P. Kúš, A. Plecenik, Fast highly-sensitive room-temperature semiconductor gas sensor based on the nanoscale Pt-TiO₂-Pt sandwich, *Sensors and Actuators B: Chemical*. 207 (2015) 351-361. <https://doi.org/10.1016/j.snb.2014.10.003>.

- [19] D. Jung, M. Han, G.S. Lee, Fast-response room temperature hydrogen gas sensors using platinum-coated spin-capable carbon nanotubes, *ACS Applied Materials & Interfaces*. 7(5) (2015) 3050-3057. <https://doi.org/10.1021/am506578j>.
- [20] A.A. Haidry, C. Cetin, K. Kelm, B. Saruhan, Sensing mechanism of low temperature NO₂ sensing with top–bottom electrode (TBE) geometry, *Sensors and Actuators B: Chemical*. 236 (2016) 874-884. <https://doi.org/10.1016/j.snb.2016.03.016>.
- [21] G.A. Hope, A.J. Bard, Platinum/titanium dioxide (rutile) interface. Formation of ohmic and rectifying junctions, *Journal of Physical Chemistry*. 87(11) (1983) 1979-1984. <https://doi.org/10.1021/j100234a029>
- [22] B. Sambandam, A. Surenjan, L. Philip, T. Pradeep, Rapid Synthesis of C-TiO₂: Tuning the Shape from Spherical to Rice Grain Morphology for Visible Light Photovatalytic Application, *ACS Sustainable Chemistry & Engineering*. 3(7) (2015) 1321-1329. <https://doi.org/10.1021/acssuschemeng.5b00044>
- [23] Ş. Altın, F. Dumludağ, Ç. Oruç, A. Altındal, Influence of humidity on kinetics of xylene adsorption onto ball-type hexanuclear metallophthalocyanine thin film, *Microelectronic Engineering*. 134 (2015) 7-13. <https://doi.org/10.1016/j.mee.2015.01.009>. (2021) 25472-25482. <https://doi.org/10.1021/acсами.1c02050>
- [24] J.H Bang, Ali Mirzaei, S.M. Han, H.Y Lee, K.Y. Shin, S.S. Kim, H.W. Kim, Realization of low-temperature and selective NO₂ sensing of SnO₂ nanowires via synergistic effects of Pt decoration and Bi₂O₃ branching, *Ceramics International*. 47(4) (2021) 5099-5111. <https://doi.org/10.1016/j.ceramint.2020.10.088>
- [25] M.M. Abramova, N.A. Enikeev, R.Z. Valiev, A. Etienne, B. Radiguet, Y. Ivanisenko, X. Sauvage, Grain boundary segregation induced strengthening of an ultrafine-grained austenitic stainless steel, *Materials Letters*. 136 (2014) 349-352. <https://doi.org/10.1016/j.matlet.2014.07.188>.
- [26] A. Haidry, P. Schlosser, P. Durina, M. Mikula, M. Tomasek, T. Plecenik, T. Roch, A. Pidik, M. Stefecka, J. Noskovic, M. Zahoran, P. Kus, A. Plecenik, Hydrogen gas sensors based on nanocrystalline TiO₂ thin films, *Open Physics*. 9(5) (2011) 1351-1356. <https://doi.org/10.2478/s11534-011-0042-3>.

- [27] A.A. Haidry, N. Kind, B. Saruhan, Investigating the influence of Al-doping and background humidity on NO₂ sensing characteristics of magnetron-sputtered SnO₂ sensors, *Journal of Sensors and Sensor Systems*. 4(2) (2015) 271-280. <https://doi.org/10.5194/jsss-4-271-2015>.
- [28] A.A. Haidry, L. Xie, Z. Wang, Z. Li, Hydrogen sensing and adsorption kinetics on ordered mesoporous anatase TiO₂ surface, *Applied Surface Science*. 500(2020) 144219. <https://doi.org/10.1016/j.apsusc.2019.144219>.
- [29] R.L. Tseng, F.C. Wu, R.S. Juang, Characteristics and applications of the Lagergren's first-order equation for adsorption kinetics, *Journal of the Taiwan Institute of Chemical Engineers*. 41(6) (2010) 661-669. <https://doi.org/10.1016/j.jtice.2010.01.014>.
- [30] C.R. Doering, D. ben-Avraham, Interparticle distribution functions and rate equations for diffusion-limited reactions, *Physical Review A*. 38(6) (1988) 3035-3042. <https://doi.org/10.1103/physreva.38.3035>.
- [31] C. Aharoni, F. Tompkins, Kinetics of adsorption and desorption and the Elovich equation, *Advances in Catalysis*. 21(1970) 1-49. [https://doi.org/10.1016/S0360-0564\(08\)60563-5](https://doi.org/10.1016/S0360-0564(08)60563-5)
- [32] Y.S. Ho, G. McKay, Pseudo-second order model for sorption processes, *Process Biochemistry*. 34(5) (1999) 451-465. [https://doi.org/10.1016/S0032-9592\(98\)00112-5](https://doi.org/10.1016/S0032-9592(98)00112-5)
- [33] S. Lagergren, Zur theorie der sogenannten adsorption gelöster stoffe, (1898) 1-39.
- [34] R.S. Juang, M.L. Chen, Application of the Elovich equation to the kinetics of metal sorption with solvent-impregnated resins, *Industrial & Engineering Chemistry Research*. 36(3) (1997) 813-820. <https://doi.org/10.1021/ie960351f>
- [35] F.C. Wu, R.L. Tseng, R.S. Juang, Characteristics of Elovich equation used for the analysis of adsorption kinetics in dye-chitosan systems, *Chemical Engineering Journal*. 150(2-3) (2009) 366-373. <https://doi.org/10.1016/j.cej.2009.01.014>
- [36] J.P. Simonin, On the comparison of pseudo-first order and pseudo-second order rate laws in the modeling of adsorption kinetics, *Chemical Engineering Journal*. 300 (2016) 254-263. <https://doi.org/10.1016/j.cej.2016.04.079>.
- [37] Y.S. Ho, Absorption of heavy metals from waste streams by peat, University of Birmingham, 1995.
- [38] Y.S. Ho, D.A.J. Wase, C.F. Forster, Batch nickel removal from aqueous solution by sphagnum moss peat, *Water Research*. 29(5) (1995) 1327-1332. [https://doi.org/10.1016/0043-1354\(94\)00236-Z](https://doi.org/10.1016/0043-1354(94)00236-Z)

- [39] J. Sobkowski, A. Czerwiński, Electrochemistry, Kinetics of carbon dioxide adsorption on a platinum electrode, *Journal of Electroanalytical Chemistry and Interfacial Electrochemistry*. 55(3) (1974) 391-397. [https://doi.org/10.1016/S0022-0728\(74\)80433-X](https://doi.org/10.1016/S0022-0728(74)80433-X)
- [40] G. Blanchard, M. Maunaye, G. Martin, Removal of heavy metals from waters by means of natural zeolites, *Water Research*. 18(12) (1984) 1501-1507. [https://doi.org/10.1016/0043-1354\(84\)90124-6](https://doi.org/10.1016/0043-1354(84)90124-6)
- [41] X. Guo, J. Wang, A general kinetic model for adsorption: Theoretical analysis and modeling, *Journal of Molecular Liquids*. 288 (2019) 111100. <https://doi.org/10.1016/j.molliq.2019.111100>.
- [42] Y.S. Ho, G. McKay, Comparative sorption kinetic studies of dye and aromatic compounds onto fly ash, *Journal of Environmental Science and Health, Part A*. 34(5) (1999) 1179-1204. <https://doi.org/10.1080/10934529909376889>.
- [43] Y.S. Ho, G. McKay, A Comparison of Chemisorption Kinetic Models Applied to Pollutant Removal on Various Sorbents, *Process Safety and Environmental Protection*. 76(4) (1998) 332-340. <https://doi.org/10.1205/095758298529696>.
- [46] Y.S. Ho, G. McKay, D.A.J Wase, C.F. Forster, Study of the sorption of divalent metal ions on to peat, *Adsorption Science & Technology*. 18(7) (2000) 639-650. <https://doi.org/10.1260/0263617001493693>
- [45] Y.S. Ho, Using of "pseudo-second-order model" in adsorption, *Environmental Science and Pollution Research*. 21(11) (2014) 7234-72355. <https://doi.org/10.1007/s11356-013-2213-9>.